Metals

CrossMark

On nanostructured molybdenum–copper composites produced by high-pressure torsion

Julian M. Rosalie[1,*], Jinming Guo[1], Reinhard Pippan[1], and Zaoli Zhang[1]

[1] *Erich Schmid Institute, Austrian Academy of Sciences, Jahnstrasse 12, 8700 Leoben, Austria*

ABSTRACT

Nanostructured molybdenum–copper composites have been produced through severe plastic deformation of liquid-metal infiltrated Cu30Mo70 and Cu50Mo50 (wt%) starting materials. Processing was carried out using high-pressure torsion at room temperature with no subsequent sintering treatment, producing a porosity-free, ultrafine-grained composite. Extensive deformation of the Cu50Mo50 composite via two-step high-pressure torsion produced equiaxed nanoscale grains of Mo and Cu with a grain size of 10–15 nm. Identical treatment of Cu30Mo70 produced a ultrafine, lamellar structure, comprised of Cu and Mo layers with thicknesses of ~ 5 and $\sim 10-20$ nm, respectively, and an interlamellar spacing of 9 nm. This microstructure differs substantially from that of HPT-deformed Cu–Cr and Cu–W composites, in which the lamellar microstructure breaks down at high strains. The ultrafine-grained structure and absence of porosity resulted in composites with Vickers hardness values of 600 for Cu30Mo70 and 475 for Cu50Mo50. The ability to produce Cu30Mo70 nanocomposites with a combination of high-strength, and a fine, oriented microstructure should be of interest for thermoelectric applications.

Introduction

Molybdenum–copper composites are used in high-power electrical applications such as thermoelectrics where a combination of dimensional stability, high mechanical strength and high thermal and electrical conductivity are required [1–3]. Molybdenum has the high melting point (2610 °C [4]) and low thermal expansion coefficient [5] characteristic of refractory metals such as Nb, Ta, W and Cr. While molybdenum has similar electrical and thermal conductivity to tungsten, the lower density of Mo makes it preferred for weight-critical applications [5] and its lower ductile-to-brittle transformation temperature (DBTT) of ~ 373 K [6] makes forming Mo–Cu composites easier than equivalent Cu–W composites. In addition to providing the composites with thermal and electrical conductivity, copper also increases the ductility of the composites [5, 7] which is useful both during production and in service.

Mo and Cu have a positive enthalpy of mixing of +18 Kj/mol and have negligible solid solubility even

---

at the melting temperature of copper [8]. The lack of mutual solubility is advantageous for retaining high conductivity [3, 9]; however, it also results in a weak interface and hence poor mechanical bonding between the phases [10].

Mo–Cu composites are conventionally produced via liquid-metal infiltration [5, 11]. This involves sintering Mo powders to make a porous preform which can then be infiltrated with molten Cu. This process is only viable in a limited composition range, and the rate of densification is low [12].

Efforts to accelerate densification have mainly involved using ball milling to produce nanoscale Mo and Cu powders with high defect concentrations. These can then be densified more rapidly via powder compaction and sintering at 1000–1200 °C [12–14]. Although the ball-milled powders have grain sizes in the range of 10–20 nm, grain growth during sintering is rapid and the densified compacts have grain diameters of several microns [3, 11, 13]. Complete densification remains unachievable and intergranular porosity is still observed after sintering [3, 13].

High-pressure torsion (HPT) has been used for grain refinement and mechanical alloying of a wide range of Cu-based systems including Cu–Fe [15–17], Cu–Cr [18, 19], Cu–Nb [20, 21] and Cu–W [22, 23]. Deformation is carried out under quasi-hydrostatic conditions, allowing brittle materials such as refractory metals to be extensively strained without the need for external heating. This, in turn, avoids the grain growth which accompanies high-temperature sintering. Previous studies on pure Mo found more extensive grain refinement could be achieved with HPT (with an average grain size of $0.2 \, \mu m$) than with either equal channel angular extrusion (ECAE) or multi-stage forming (average grain sizes of 2.5 and $1.8 \, \mu m$, respectively) due to the lower processing temperature [24]. HPT imposes a strain that is proportional to the radial distance at a given point, and thus, a single sample can provide information covering a wide range of strain conditions.

The objective of this investigation was to use HPT to produce bulk, full-dense, nanograined Mo–Cu composites and to examine their microstructures at different applied strains. Although there are number of reports on the HPT deformation of the related Cu–Cr (see for example, [18, 19, 25]) and several on Cu–W [22, 23] systems, to the best of the authors' knowledge this work provides the first examination of HPT-deformed Cu–Mo composites.

Experimental details

This investigation was carried out using two liquid-metal infiltrated Mo–Cu composites provided by Plansee SE, Austria. These composites had compositions of Mo-30 wt% Cu (40 at.% Cu) and Mo-50 wt% Cu (60 at.% Cu). These are hereafter described as Cu30Mo70 and Cu50Mo50, respectively.

Deformation was applied using multi-step high-pressure torsion (HPT) [17]. Discs (height, $h \sim 12 \, mm$, diameter, $\phi = 30 \, mm$) were cut from the raw ingots by electrical discharge machining. These were deformed at room temperature in a 4000 kN HPT apparatus, using tool steel anvils with an anvil gap of 3.5 mm. A total of either 5 or 10 complete rotations (hereafter described as $N_1 = 5$ or 10, with the subscript indicating the first step of deformation) were performed at an angular velocity (ω) of 0.0625 revolutions per minute (rpm) under an applied pressure of $\sim 4.5 \, GPa$.

Cylindrical samples ($h \sim 20 \, mm$, $\phi = 7.5 \, mm$) were cut from the discs, perpendicular to the shear plane of this disc (see Fig. 1). These cylinders were sectioned into samples with height $\sim 1.1 \, mm$. The average strain in these discs was calculated as 25 for $N_1 = 5$ and 50 for $N_1 = 10$. Step 2 deformation was conducted using a 400 kN HPT apparatus at an applied pressure of 7.4 GPa and $\omega = 0.4 \, rpm$. The second step of deformation consisted of $N_2 = 10 - 50$ rotations of deformation with a 0.25 mm anvil gap and cavity diameter of 8 mm.

Vickers microindentation hardness testing was conducted on as-received material and following each step of HPT deformation. Scanning electron microscopy was used to characterise the microstructure in the as-received condition and following HPT deformation. Samples for SEM examination were ground and polished using standard techniques, within final polishing taking place on a Buehler Vibromet polisher. SEM examinations were carried out using a Zeiss Leo 1525 microscope equipped with field emission gun and Gemini lens system. Micrographs were recorded using the backscattered electron detector (BSD) with source voltages of 15–20 kV. Stereological measurements were taken using ImageJ software (Version 1.50g). The Mo particle size in the as-received condition was measured by a processing consisting of (i) background subtraction, (ii) thresholding, (iii) separation of connected particles via the watershed algorithm and (iv) measurement of the
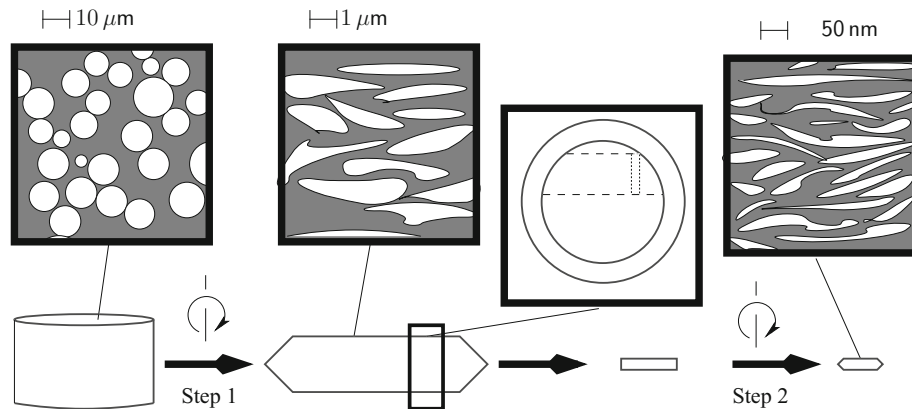
Figure 1 Schematic representation of the sample geometry and corresponding microstructure at each stage of processing. The microstructures produced by step 1 and step 2 HPT deformation are described in detail in the following section. Note that the shear plane during step 2 HPT is perpendicular to that of step 1 deformation.

projected particle area. Determining the lamellar spacing required similar preprocessing steps of background subtraction and thresholding. The spacing was then measured by counting the number of intercepts using a circular grid to give the true mean spacing [26]. This follows the established methodology developed for measuring lamellar spacings in pearlitic steels.

Cross-sectional and plan-section TEM foils prepared by dimple grinding to a thickness of 10–15 μm, followed by precision ion polishing (PIPS) to perforation using a Gatan 691 instrument. For planar samples (see Fig. 2), the electron beam is oriented normal to the shear plane, whereas for cross-sectional samples, the electron beam is oriented parallel to this plane. Note that in both cases, electron beam is normal to the shear direction and elongation of the components will be visible. PIPS made use of a liquid nitrogen-cooled sample stage to minimise specimen heating during foil preparation. The foils examined were extracted from the outer section of the HPT disc,
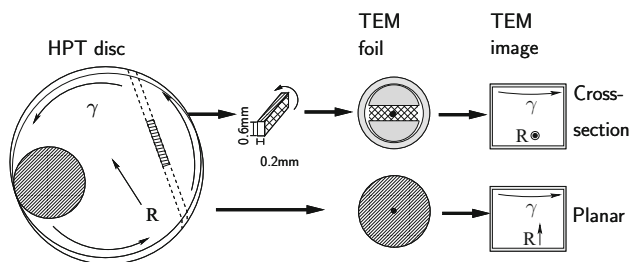
and the hole position corresponds to a radial distance of approximately 3 mm. TEM and scanning TEM (STEM) observations were made using CM12 and JEOL Cs-corrected 2100F microscopes operating at 120 and 200 kV, respectively. High-angle annular dark-field STEM (HAADF-STEM) images were obtained on the JEOL microscope with inner and outer collection angles of 65.51 and 174.9 mrad, respectively. Lamellar spacings were determined from the STEM images using the same procedure as for the SEM micrographs. It was not possible to obtain reliable data from heavily deformed Cu50Mo50 composites due to the decomposition of the lamellar structure, as is described in the following section.

Results

Hardness testing

The Vickers microindentation hardness after step 1 and step 2 HPT deformation is shown in Fig. 3a and b, respectively. Values for the as-received Cu30Mo70 and Cu50Mo50 alloys are shown on the plot, along with values measured for pure Cu and Mo. The strain values are given as the von Mises strain (Eq. 1) for each stage of deformation (i.e. γ_1 and γ_2, respectively). Assuming that slippage is negligible, the equivalent strain (γ_{eq}) after N rotations at a radial distance r is given by,

$$\gamma_{eq} \cong \frac{2\pi r N}{\sqrt{3}t} \tag{1}$$

Figure 2 Schematic showing the relationship between the HPT disc and the orientation of the planar and cross-sectional TEM samples. For both sample types, the shear direction is normal to the electron beam.
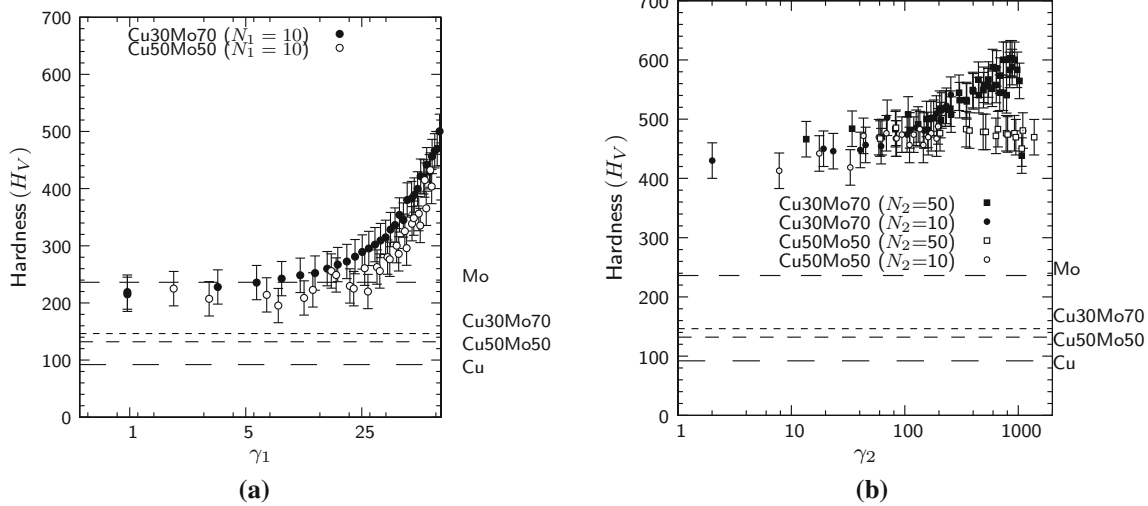
Figure 3 Vicker's indentation hardness of HPT Cu50Mo50 and Cu30Mo70 alloys as a function of shear strain after **a** step 1 and **b** step 2 HPT deformation. Strain values are indicated by γ_1 and γ_2, respectively. Hardness values for the as-received Cu30Mo70 and Cu50Mo50 alloys are shown, along with values measured for pure Cu and Mo.

where the disc thickness is t [27]. In the ideal case where co-deformation of both phases occurs, and slippage is absent, the strains in each step are multiplicative [17] giving a total equivalent strain of ~ 50000 for the maximum deformation used in this work ($N_1 = 10$, $N_2 = 50$).

The hardness of both alloys increased rapidly during the first step of HPT deformation, to reach 400 H_V in the case of Cu50MoZand 420 for Cu30Mo70 (Fig. 3a). The curves for both alloys are similar and show the typical increase in hardness with applied strain (i.e. at greater distances from the centre of rotation), but with the Mo-rich composition showing a slightly higher hardness at equivalent levels of strain.

Differences between the two compositions become more evident during step 2 HPT deformation. For Cu50Mo50, the least strained region (close to the neutral strain axis) showed no increase over the maximum value during step 1 deformation. In the remainder of the disc, the hardness increased to a plateau at 475 H_V after $N_2 = 10$ rotations, with no further increase when 50 rotations were applied.

In contrast, the Cu30Mo70 had a considerable increase in hardness during step 2 deformation with a substantial difference in hardness remaining between the highly strained edges and the lesser strained central region. The overall hardness increased further for 50 rotations as compared to 10 rotations. After step 2 HPT (50 rotations), the

hardness of Cu30Mo70 ranged from 480 to 600 H_V. This was a substantial increase over the as-received condition, in which the hardness was measured as $146 \pm 4\,H_V$ and pure Mo ($236 \pm 4\,H_V$). The wide range of hardness values and lack of a plateau region indicated that this material had not yet reached a strain-saturated condition.

Scanning electron microscopy

Scanning electron micrographs of the as-received composites showed a network of connected, spheroidal Mo particles. The micrographs shown were obtained using backscattered electron mode in which Cu (atomic no., $Z = 29$) appears dark and Mo ($Z = 42$) appears bright. In each of the micrographs, the shear plane is horizontal and lies normal to the plane of the page. The main distinction between the two compositions was a higher number of Cu-filled pores with diameters of 10–50 μm diameter in the Cu50Mo50 alloy (Fig. 4a, b). Voids of approximately 1 μm in diameter are apparent in several of the Mo particles in the higher-magnification images shown in Figs. 4c, d.

Stereological measurements were taken to determine the distribution of projected areas of the Mo particles, as shown in Fig. 5. Assuming a spherical particle geometry, the data yielded average diameters of 3.8 μm for Cu30Mo70 and 5.0 μm for Cu50Mo50. The particles were relatively monodisperse; in the

Figure 4 Backscattered electron micrographs of as-received **a**, **c** Cu50Mo50 and **b**, **d** Cu30Mo70 showing the interconnected network of Mo particles infiltrated by copper.

Cu50Mo50   Cu30Mo70

(a)   (b)

(c)   (d)
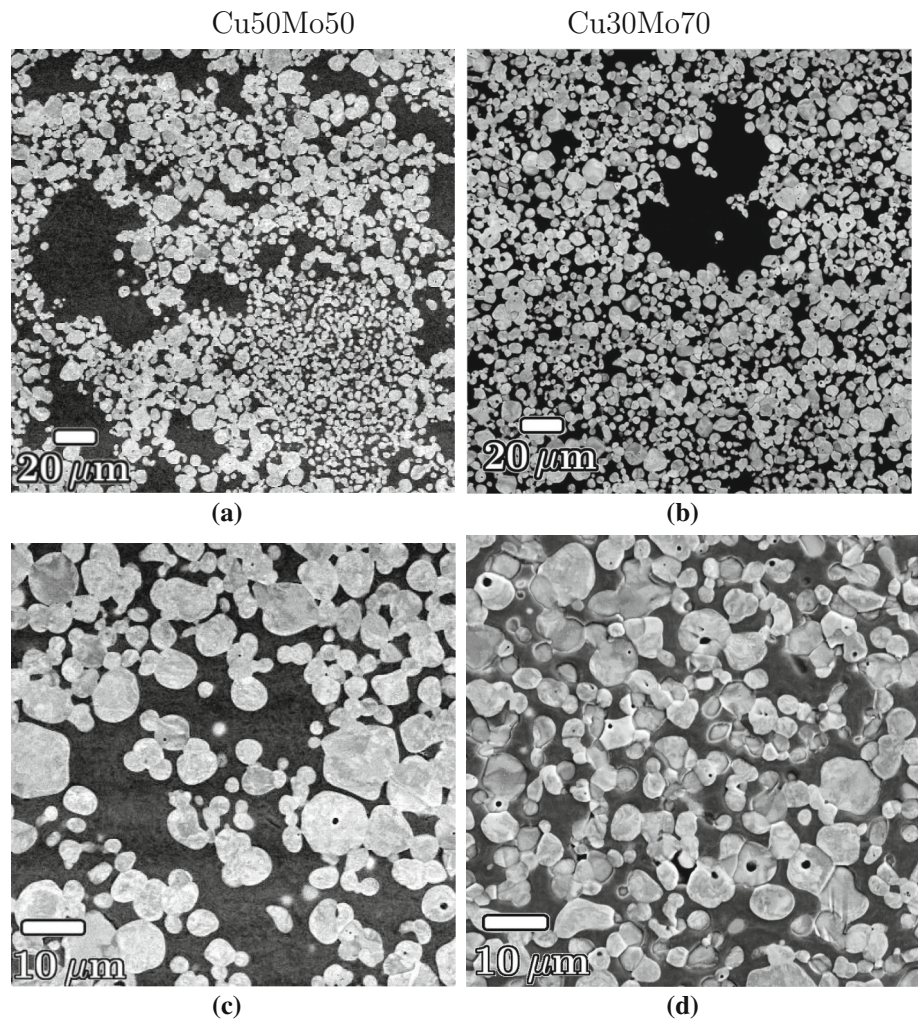
case of Cu30Mo70, 50% of Mo particles had diameters between 2.3 and 4.3 μm. For the Cu50Mo50 composite, the equivalent values were 2.8 and 5.7 μm.

A lamellar microstructure began to develop during step 1 HPT deformation. Figure 6 presents typical micrographs obtained at this step of deformation, with the shear direction in the horizontal plane of the page. The development of a lamellar microstructure can be seen by comparing images recorded at the centre of the samples (Fig. 6a, c) where the local strain is minimal (and theoretically zero at the exact rotation axis) and those recorded at the outer rim of the sample (Fig. 6b, d) where the maximum strain was imposed. The lamellae were finer in the Mo-rich composition and could be identified at lower strain. For example, a lamellar structure is already visible at the centre of the Cu30Mo70 composite (Fig. 6c) but not in Cu50Mo50 (Fig. 6a), although some co-deformation is evident.
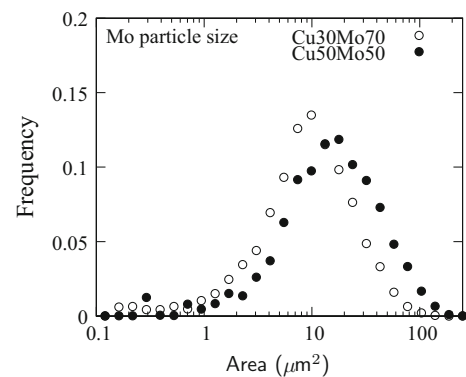

Figure 5 Stereological measurements of the projected area of the Mo particles in the as-received composites.

Backscattered electron micrographs of samples given step 2 deformation showed uniform brightness with no lamellae or individual grains being identified. The absence of well-defined changes in atomic

contrast was taken as evidence that either (a) a single-phase microstructure had developed or (b) that microstructure was of a finer scale than the interaction volume of the SEM could resolve. This required recourse to transmission electron microscopy to determine and is discussed in the following section.

Transmission electron microscopy

TEM micrographs of Cu30Mo70 subjected to two-step deformation show a microstructure comprised of lamellae with a thickness of 5–20 nm. Figure 7a shows a typical region of a foil of Cu30Mo70 after two-step HPT deformation ($N_1 = 10$, $N_2 = 50$) corresponding to equivalent strains $\gamma_1 \approx 50$, $\gamma_2 \approx 750$. The shear plane in both micrographs is angled from top right to bottom left and lies normal to the plane of the page. The selected area diffraction pattern (inset) shows reflections attributable to both phases.

Figure 7b shows a high-resolution TEM image showing a series of alternating Cu and Mo lamellae. The central Cu region is viewed along the [011] zone axis, and both the adjacent Mo lamellae are close to this orientation.

Mo- and Cu-rich regions are readily distinguished in high-angle annular dark-field (HAADF) scanning transmission electron microscope (STEM) images. Mo lamellae (bright regions in the micrograph) were 10–20 nm in thickness, whereas the (darker) Cu lamellae were generally ~5 nm in thickness. Figure 8 presents a series of typical bright-field and HAADF-STEM images of Cu30Mo70 after step 2 HPT deformation. Both Cu and Mo lamellae are highly elongated, with lengths of 200 nm or longer, and are aligned closely with the shear plane which is normal to the plane of the page and is oriented horizontally in (a, b) and from top left to bottom right in (c,d).

Figure 6 Backscattered electron micrographs of **a**, **c** Cu50Mo50 and **b**, **d** Cu30Mo70 showing the lamellar structure after step 1 HPT deformation (10 rotations, $\gamma_1 \approx 70$). Mo (atomic number, Z = 42) appears bright, with Cu-containing (Z = 29) regions appearing *dark*.
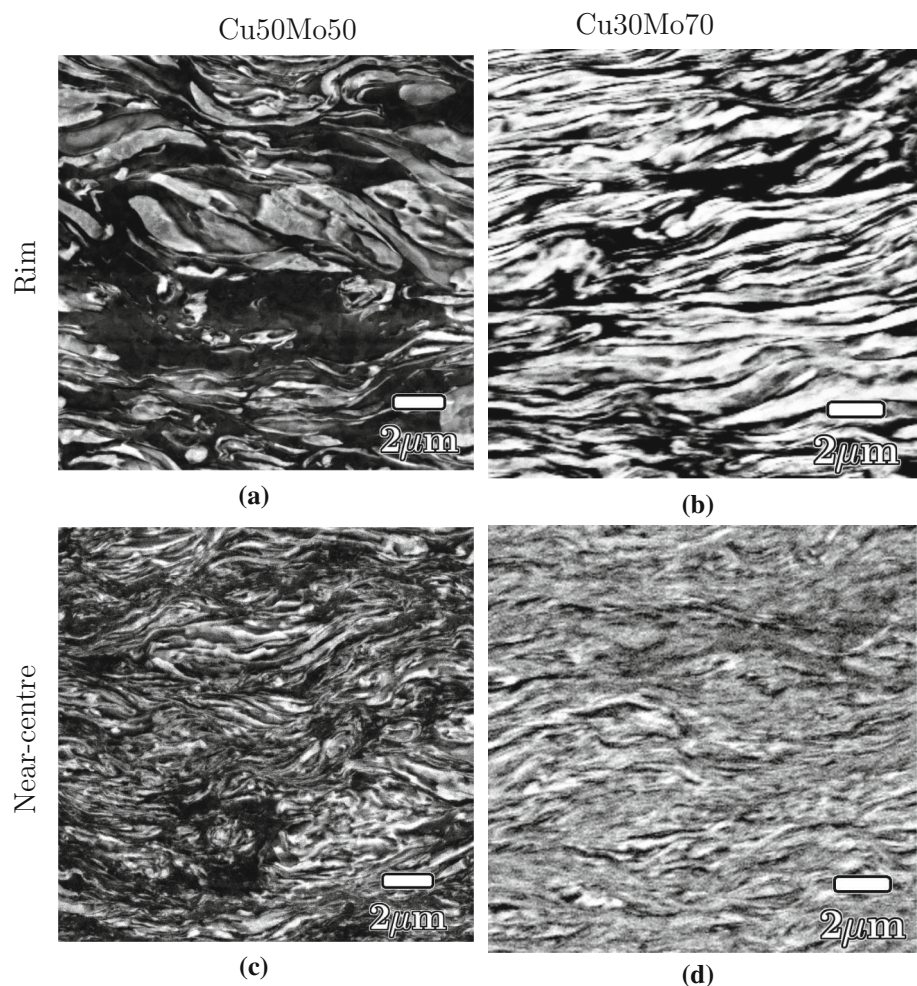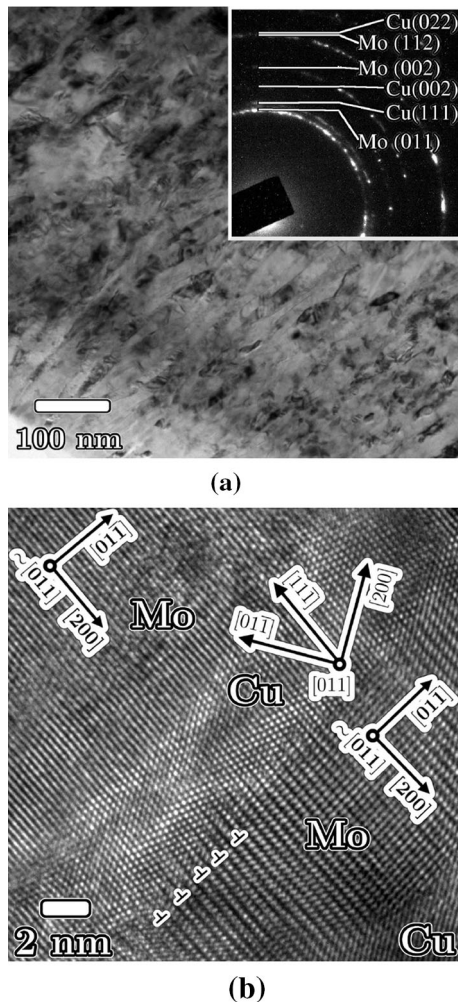
Figure 7 TEM images of Cu30Mo70 after two-step HPT deformation ($\gamma_2 \approx 750$). **a** Shows a bright-field, diffraction contrast image giving an overview of the microstructure. **b** Shows a high-resolution image showing alternating copper and molybdenum lamellae.

Stereological measurements of the lamellar spacing using circular grids gave a lamellar spacing of 9 nm.

The microstructure of the Cu50Mo50 alloy did not remain lamellar after the second step of HPT deformation. HAADF-STEM micrographs of Cu50Mo50 show equiaxed Mo grains with diameters of approximately 10–15 nm (Fig. 9). The Mo particles (appearing as darker regions in (a, c) and bright regions in the HAADF-STEM images (b, d) appear to be embedded within the Cu component, with a separation of <5 nm between adjacent Mo particles. There appeared to be no relationship between the particle morphology and the shear plane which lies in the horizontal plane.

Discussion

Liquid-metal infiltrated Mo–Cu proved to be amenable to room-temperature deformation via HPT, making it possible to produce nanometre-scale composites. No radial cracking was observed after step 1 deformation, where the maximum equivalent strain was ∼72. Although radial cracks were sometimes evident after step 2 deformation, it was generally possible to deform to 50 revolutions. Deformation-induced heating during HPT is only expected to raise the temperature to around 373K during step 1 deformation and 300K during step 2 deformation. This is much lower than the temperatures of 573–673 K [6] usually required to ensure sufficient ductility in Mo; however, the high imposed pressure and quasi-hydrostatic conditions allowed for deformation of both Cu and Mo components.

Due to the fine scale of the HPT material and the absence of intergranular porosity, the hardness values in the strain-saturated state compare very favourably with densified ball-milled materials. The hardness values reported in Mo–Cu with Mo < 20 wt% alloys were in the range of 200–259 H_V [3, 28, 29], and ball-milled and annealed pure Mo was reported to have a hardness of 250 H_V. These values are substantially below the values of 475 and 600 H_V measured herein for HPT-deformed Cu50Mo50 and Cu30Mo70, respectively.

Both of the Cu–Mo composites developed similar lamellar microstructures during the first step of deformation (Fig. 6), with the microstructure being more refined at higher strains (c,d) and in the Cu30Mo70 composite for equal strain (b, d). However, in the Cu50Mo50 composite, this microstructure decomposes during step 2 deformation in Cu50Mo50 (Fig. 9) unlike Cu30Mo70 (Fig. 8). Previous investigations on binary systems containing phases with substantial differences in hardness have reported the lamellar structure formed during HPT break-up at higher strains and is replaced by a microstructure consisting of equiaxed grains [18]. It has been argued that once such microstructures develop, additional deformation is localised in the softer phase and does not further refine the microstructure [18]. The microstructure then enters a steady state, with the mechanical properties, including hardness, remaining unchanged even if further strain is applied. Strain localisation in the soft phase occurs more readily for small volume fractions of the hard phase, where there

Figure 8 **a**, **c** Bright-field and **b**, **d** HAADF-STEM images of Cu30Mo70 after two-step HPT deformation ($\gamma_2 \approx 750$). Mo-rich regions appear bright in **b**, **d**.
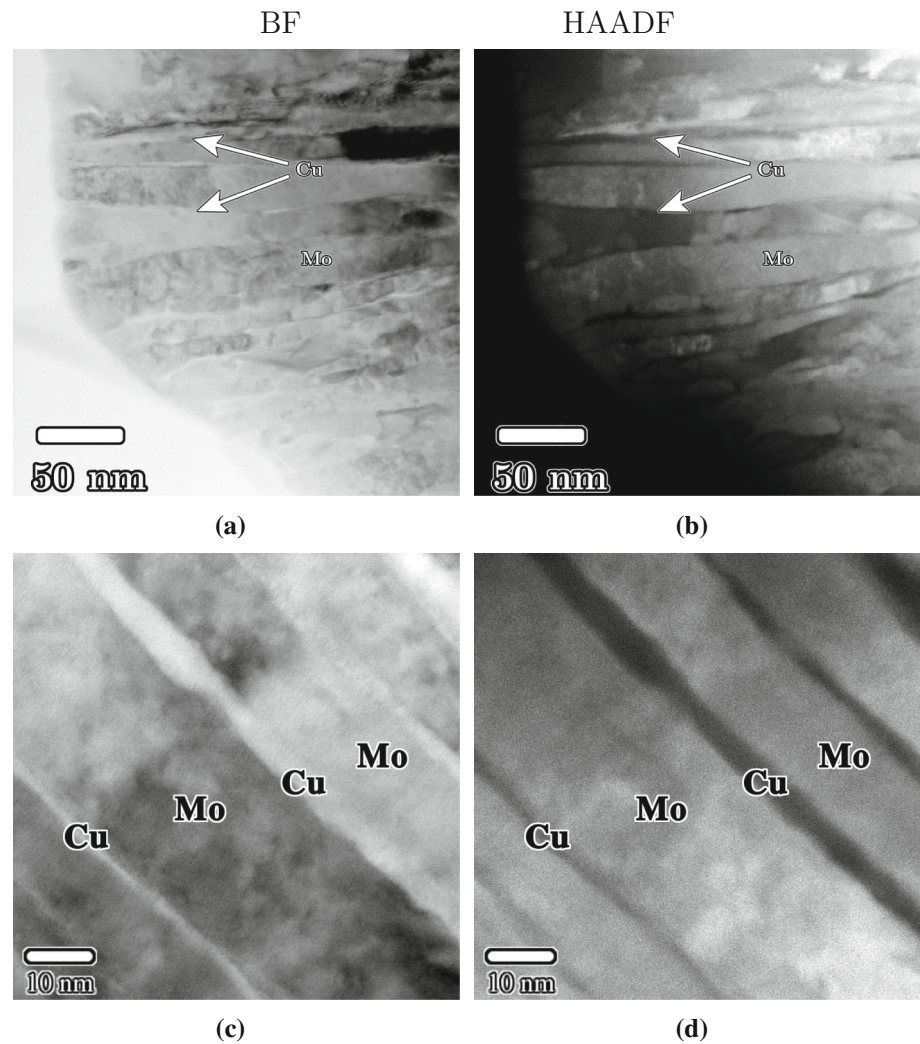

is limited contact between particles of the hard phase during deformation. Therefore, the higher volume fraction of Mo in Cu30Mo70 (67% compared to 47% in Cu50Mo50) is thought to be responsible for the retention of a lamellar structure even after extensive two-step deformation.

The relationship between the hardness and lamellar spacing (s), of the composites is presented in Fig. 10, which shows a Hall–Petch dependence on the lamellar spacing for spacings as low as 160 nm. The gradient of the hardness values plotted against $1/\sqrt{s}$ for lamellar spacing s, gave a Hall–Petch coefficient, K, of $217 \pm 7\,\mathrm{MPa}/\mu\mathrm{m}^{1/2}$. Similar relationships between lamellar spacing and hardness were demonstrated in eutectoid pearlitic steels [30] and have also been established for the widely studied Cu–Nb composites [31–34]. This behaviour indicates that plastic deformation is interface controlled, due to the

difficulty of transferring dislocations across the interface. However, further refinement of the microstructure had little effect, with a factor of 20 reduction in the spacing leading to a hardness increase of approximately 20%. This deviation from the Hall–Petch relationship for extremely fine structures has been reported in nanoscale Cu–Nb alloys [35]. This is thought to indicate a change in the deformation mechanism, with studies suggesting that interface sliding occurs [36].

The microstructural development of the Cu–Mo composites is initially similar to that reported for HPT deformation of other Group VI refractory metals. HPT deformation of a W-25 wt% Cu composite resulted in a lamellar microstructure for equivalent strains of at least 64 [37]. Another study using a two-step HPT procedure subjected W-25 wt% Cu to equivalent strains of 1000 without reaching a

Figure 9 **a**, **c** Bright-field and
b, **d** HAADF-STEM images
of Cu50Mo50 after two-step
HPT deformation ($\gamma_2 = 750$).
Mo-rich regions appear bright
in **b**, **d**.

BF   HAADF

(a)   (b)

(c)   (d)
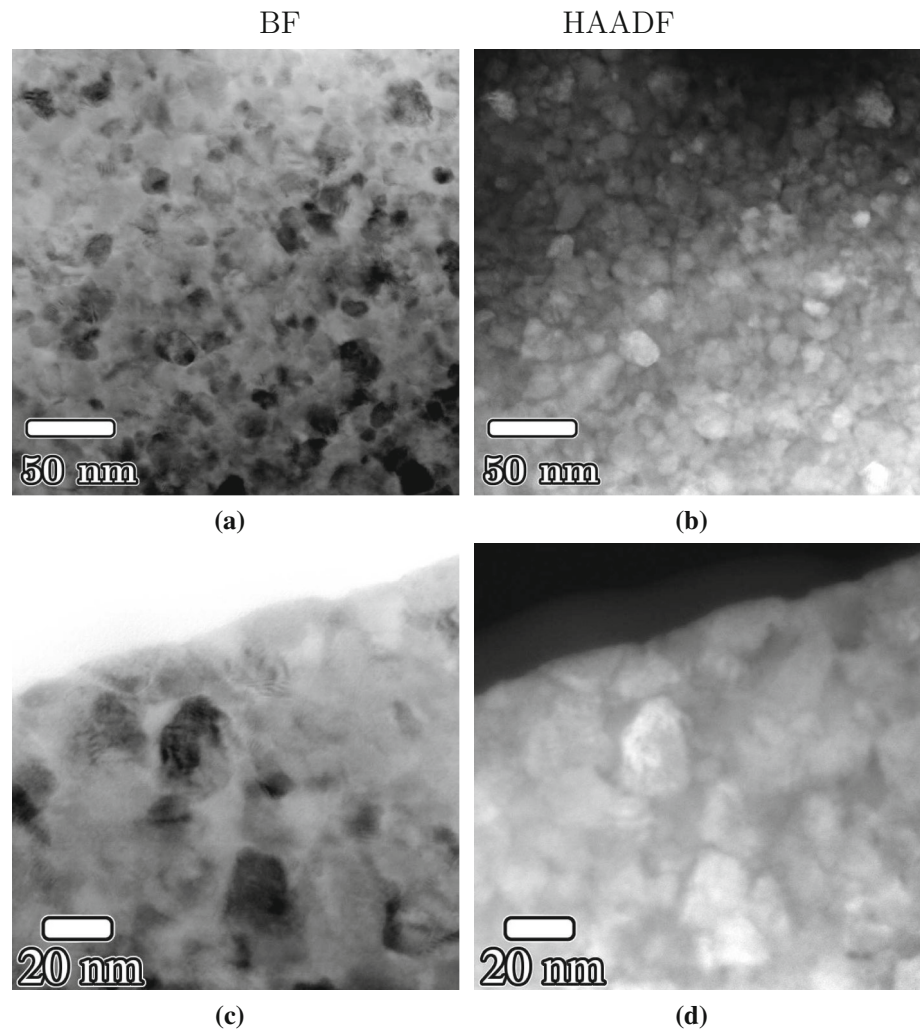
hardness plateau [23]. This would suggest that the material retains a lamellar microstructure under these conditions. HPT Cu–Cr composites have also been examined at high strains [18, 38], and it has been shown that the lamellar structure decomposed to form equiaxed, roughly spheroidal particles after strains of ∼250 [38]. These reached a grain size of ∼15 nm after strain of ≈1400 but showed no further reduction in grain size at a strain of ≈4000 [39]. In comparison, an average equivalent shear strain of ∼50 was imposed on the Cu–Mo composites during the first HPT deformation step and a further (multiplicative) strain of ∼1000 during the second deformation step, indicating the Cu30Mo70 layered microstructure is stable to extremely high strains.

The deformability of the refractory phase at a given temperature and hence the ductile-to-brittle transformation temperature are also critical to the retention of the lamellar microstructure. The DBTT of tungsten (370–470 K [40]) is only slightly higher than the value of ∼373 K [6] for Mo. However, chromium has a DBTT variously reported between 423 and 773 K [41–43], and in Cu–Cr composites, the lamellar structure decomposes at much lower strains than either Cu–W or Cu–Mo.

Composites with similar layer thicknesses of ∼10−20 nm layers have also produced via accumulative roll bonding (ARB) of pure Cu and Nb [20, 44]. These layered structures were retained during subsequent HPT deformation of the ARB composite [20]. It is important to note, however, that molybdenum is significantly less ductile than niobium and that the quasi-hydrostatic conditions during HPT play a role in allowing for Mo/Cu co-deformation at room temperature. HPT therefore offers a means of generating ultrafine layered structures containing less
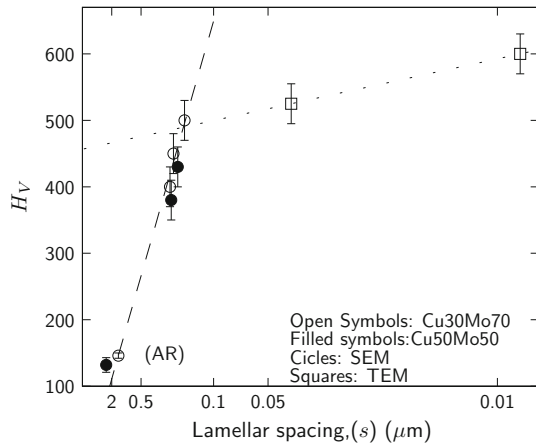
Figure 10 Hardness of the Cu–Mo composites plotted against the lamellar spacing s. A Hall–Petch coefficient of $K = 217 \pm 7\,\mathrm{MPa}/\mu\mathrm{m}^{1/2}$ was determined from the gradient for $s > 160\,\mathrm{nm}$. The *line* for $s < 160\,\mathrm{nm}$ is provided as a guide for the eye only.

ductile refractory elements, opening up the possibility of more detailed studies of their microstructure and properties. One area of interest concerns the texture of the composites, since the ARB Cu–Nb composites evolved atypical textures as the layer thickness approached the grain size due to the increasing influence of interfaces and the constraint imposed by neighbouring grains [44]. Further work is underway to examine the texture of Cu–Mo HPT composites.

Conclusions

Liquid-metal infiltrated Mo–Cu composites were found to be amenable to high-pressure torsion at room temperature. Both copper and molybdenum phases underwent deformation, giving a lamellar microstructure after the first step of HPT deformation, corresponding to an average equivalent shear strain of 50. In Cu50Mo50, the lamellar structure breaks up during the second step of HPT deformation and the microstructure consisted of equiaxed Mo nanoscale grains surrounded by Cu. This behaviour is similar to that of Cu–Cr composites and liquid-metal infiltrated Cu–W composites and is associated with a strain-saturated state in which the hardness reaches a plateau. However, in the Cu30Mo70 material, the lamellar structure was retained, and after stage-two deformation, the resulting composites had a fine lamellar structure with Cu and Mo forming

5 nm and 10–20 nm lamellae, respectively, with an overall lamellar spacing of 9 nm. Notwithstanding the poor room-temperature ductility of Mo, this microstructure was stable to equivalent strains of ~ 50000 and the layer thicknesses became equivalent to those of accumulative roll-bonded Cu–Nb. Since no sintering was used, post-deformation grain growth was avoided. The fine microstructure and absence of porosity contributed to Vickers hardness values of 475 for Cu50Mo50 and 600 for Cu30Mo70. The combination of high-strength, and a fine, oriented microstructure would be well suited to thermoelectric materials and shows that HPT-deformed Cu–Mo composites warrant further investigation for such applications.

References

[1] Aguilar C, Guzman D, Rojas PA, Ordonez S, Rios R (2011) Simple thermodynamic model of the extension of solid solution of Cu–Mo alloys processed by mechanical alloying. Mater Chem Phys 128(3):539–542

[2] Guo S, Kang Q, Cai C, Qu X (2012) Mechanical properties and expansion coefficient of Mo–Cu composites with different Ni contents. Rare Met 31(4):368–371

[3] Kumar A, Jayasankar K, Debata M, Mandal A (2015) Mechanical alloying and properties of immiscible Cu-20 wt% Mo alloy. J Alloys Comp 647:1040–1047

[4] Cockeram BV (2002) Measuring the fracture toughness of molybdenum-0.5 pct titanium-0.1 pct zirconium and oxide dispersion-strengthened molybdenum alloys using standard and subsized bend specimens. Metall Mater Trans A 33(12):3685–3707

[5] Fang F, Zhou Y, Yang W (2014) Temperature dependent tensile and fracture behaviors of Mo10 wt% Cu composite. Int J Refract Met H 42:120–125

[6] Shields JA, Lipetzky JP, Mueller AJ (2001) Fracture toughness of 6.4 mm (0.25 inch) arc-cast molybdenum and molybdenum-TZM plate at room temperature and 300 °C. Plansee 4:187–199

[7] Fang F, Zhou Y, Yang W (2013) In-situ SEM study of temperature dependent tensile behavior of wrought molybdenum. Int J Refract Met H 41:35–40

[8] Subramanian PR, Laughlin DE (1990) Binary alloy phase diagrams, 2nd edn. ASM International, Metals Park, OH

[9] Friedel J (1956) On some electrical and magnetic properties of metallic solid solutions. Can J Phys 34(12A):1190–1211

[10] Rodriguez JA, Goodman DW (1992) The nature of the metal-metal bond in bimetallic surfaces. Science 257(5072):897–903

[11] Johnson JL, German RM (2001) Role of solid-state skeletal sintering during processing of Mo–Cu composites. Metall Mater Trans A 32(3):605–613

[12] Wang TG, Liang QC, Qin Q (2015) Microstructure and properties of Mo–Cu alloys produced by powder metallurgy. Mater Res Innov 19(5):1150–1152

[13] Tikhii GA, Kachalin NI, Belova VP, Nikitin VI (2007) Study of a Mo–Cu pseudoalloy obtained from mechanically activated charge. Met Sci Heat Treat 49(9):448–452

[14] Xi S, Zuo K, Li X, Ran G, Zhou J (2008) Study on the solid solubility extension of Mo in Cu by mechanical alloying Cu with amorphous Cr(Mo). Acta Mater 56(20):6050–6060

[15] Mojtahedi M, Goodarzi M, Aboutalebi M, Ghaffari M, Soleimanian V (2013) Investigation on the formation of CuFe nano crystalline super-saturated solid solution developed by mechanical alloying. J Alloys Comp 550:380–388

[16] Soleimanian V, Mojtahedi M, Goodarzi M, Aboutalebi MR (2014) Characterization of crystallite size, dislocation characteristics and stacking faults in nanostructured mechanically alloyed Cu-Fe system using an advanced X-ray diffraction analysis method. J Alloys Comp 590:565–571

[17] Bachmaier A, Kerber M, Setman D, Pippan R (2012) The formation of supersaturated solid solutions in Fe–Cu alloys deformed by high-pressure torsion. Acta Mater 60(3):860–871

[18] Bachmaier A, Rathmayr GB, Bartosik M, Apel D, Zhang Z, Pippan R (2014) New insights on the formation of supersaturated solid solutions in the Cu–Cr system deformed by high-pressure torsion. Acta Mater 69:301–313

[19] Islamgaliev RK, Nesterov KM, Bourgon J, Champion Y, Valiev RZ (2014) Nanostructured Cu–Cr alloy with high strength and electrical conductivity. J Appl Phys 115(194):301

[20] Ekiz EH, Lach TG, Averback RS, Mara NA, Beyerlein IJ, Pouryazdan M, Hahn H, Bellon P (2014) Microstructural evolution of nanolayered Cu–Nb composites subjected to high-pressure torsion. Acta Mater 72:178–191

[21] Abad M, Parker S, Kiener D, Primorac MM, Hosemann P (2015) Microstructure and mechanical properties of $Cu_x Nb_{1-x}$ alloys prepared by ball milling and high pressure torsion compacting. J Alloys Comp 630:117–125

[22] Raharijaona JJ, Missiaen JM, Bouvard D (2011) A phenomenological analysis of sintering mechanisms of W–Cu from the effect of copper content on densification kinetics. Metall Mater Trans A 42(8):2411–2419

[23] Krämer L, Wurster S, Pippan R (2014) Deformation behavior of Cu-composites processed by HPT. IOP Conf Ser Mater Sci Eng 63(1):012,026

[24] Ivanov K (2008) Characteristic features and thermal stability of molybdenum processed by different ways of severe plastic deformation. Mater Sci Forum 584:917–922 Trans Tech Publications

[25] Sauvage X, Jessner P, Vurpillot F, Pippan R (2008) Nanostructure and properties of a CuCr composite processed by severe plastic deformation. Scr Mater 58(12):1125–1128

[26] Voort GV, Roósz A (1984) Measurement of the interlamellar spacing of pearlite. Metallography 17(1):1–17

[27] Cubero-Sesin JM, Horita Z (2012) Powder consolidation of Al-10wt% Fe alloy by high-pressure torsion. Mater Sci Eng A 558:462–471

[28] Sabooni S, Mousavi T, Karimzadeh F (2012) Thermodynamic analysis and characterisation of nanostructured Cu(Mo) compounds prepared by mechanical alloying and subsequent sintering. Powder Metall 55(3):222–227

[29] Aguilar C, Castro F, Martinez V, Guzman D, de las Cuevas F, Lozada L, Vielma N (2012) Structural study of nanocrystalline solid solution of Cu-Mo obtained by mechanical alloying. Mater Sci Eng A 548:189–194

[30] Ray K, Mondal D (1991) The effect of interlamellar spacing on strength of pearlite in annealed eutectoid and hypoeutectoid plain carbon steels. Acta Metall Mater 39(10):2201–2208

[31] Trybus CL, Spitzig WA (1989) Characterization of the strength and microstructural evolution of a heavily cold-

rolled Cu-20-percent Nb composite. Acta Metall 37(7):1971–1981

[32] Thilly L, Lecouturier F, von Stebut J (2002) Size-induced enhanced mechanical properties of nanocomposite copper/niobium wires: nanoindentation study. Acta Mater 50(20):5049–5065

[33] Spitzig WA (1991) Strengthening in heavily deformation processed Cu-20-percent Nb. Acta Metall Mater 39(6):1085–1090

[34] Carpenter JS, Zheng SJ, Zhang RF, Vogel SC, Beyerlein IJ, Mara NA (2013) Thermal stability of Cu–Nb nanolamellar composites fabricated via accumulative roll bonding. Philos Mag 93(7):718–735

[35] Mitchell T, Lu Y, Griffin A, Nastasi M, Kung H (1997) Structure and mechanical properties of copper/niobium multilayers. J Am Ceram Soc 80(7):1673–1676

[36] Wang J, Hoagland R, Liu X, Misra A (2011) The influence of interface shear strength on the glide dislocation-interface interactions. Acta Mater 59(8):3164–3173

[37] Sabirov I, Pippan R (2005) Formation of a W-25%Cu nanocomposite during high pressure torsion. Scr Mater 52(12):1293–1298

[38] Guo J, Rosalie J, Pippan R, Zhang Z (2017a) On the phase evolution and dissolution process in Cu–Cr alloys deformed by high pressure torsion. Scr Mater 133:41–44

[39] Guo J, Rosalie J, Pippan R, Zhang Z (2017b) Revealing the microstructural evolution in Cu-Cr alloys during high pressure torsion. Mater Sci Eng A 695:350–359

[40] Gumbsch P, Riedle J, Hartmaier A, Fischmeister HF (1998) Controlling factors for the brittle-to-ductile transition in tungsten single crystals. Science 282(5392):1293–1295

[41] Wadsack R, Pippan R, Schedler B (2002) The effect of pre-deformation on the ductility of chromium. J Nucl Mater 307–311:701–704

[42] Holzwarth U, Stamm H (2002) Mechanical and thermomechanical properties of commercially pure chromium and chromium alloys. J Nucl Mater 300(23):161–177

[43] Lucon E, van Walle E, Decréton M (2001) Mechanical properties of two chromium alloys in as-received and heat-treated conditions. Fusion Eng Design 5859:767–773

[44] Beyerlein IJ, Mara NA, Carpenter JS, Nizolek T, Mook WM, Wynn TA, McCabe RJ, Mayeur JR, Kang K, Zheng S, Wang J, Pollock TM (2013) Interface-driven microstructure development and ultra high strength of bulk nanostructured Cu–Nb multilayers fabricated by severe plastic deformation. J Mater Res 28(13, SI):1799–1812